ACS OMEGA

http://pubs.acs.org/journal/acsodf

Article

Fast-Charging Anode Materials and Novel Nanocomposite Design of Rice Husk-Derived SiO_2 and Sn Nanoparticles Self-Assembled on TiO_2(B) Nanorods for Lithium-Ion Storage Applications

Thanapat Autthawong, Chawin Yodbunork, Waewwow Yodying, Ruttapol Boonprachai, Orapim Namsar, Ai-shui Yu, Yothin Chimupala, and Thapanee Sarakonsri*

Cite This: *ACS Omega* 2022, 7, 1357−1367

Read Online

ACCESS | Metrics & More | Article Recommendations | Supporting Information

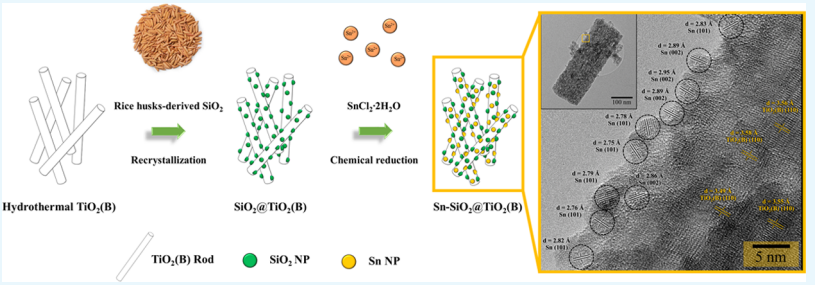

ABSTRACT: A novel microstructure of anode materials for lithium-ion batteries with ternary components, comprising tin (Sn), rice husk-derived silica (SiO_2), and bronze-titanium dioxide (TiO_2(B)), has been developed. The goal of this research is to utilize the nanocomposite design of rice husk-derived SiO_2 and Sn nanoparticles self-assembled on TiO_2(B) nanorods, Sn−SiO_2@TiO_2(B), through simple chemical route methods. Following that, the microstructure and electrochemical performance of as-prepared products were investigated. The major patterns of the X-ray diffraction technique can be precisely indexed as monoclinic TiO_2(B). The patterns of SiO_2 and Sn were found to be low in intensity since the particles were amorphous and in the nanoscale range, respectively. Small spherical particles, Sn and SiO_2, attached to TiO_2(B) nanorods were discovered. Therefore, the influence mechanism of Sn−SiO_2@TiO_2(B) fabrication was proposed. The Sn−SiO_2@TiO_2(B) anode material performed exceptionally well in terms of electrochemical and battery performance. The as-prepared electrode demonstrated outstanding stability over 500 cycles, with a high discharge capacity of ∼150 mA h g^{-1} at a fast-charging current of 5000 mA g^{-1} and a low internal resistance of around 250.0 Ω. The synthesized Sn−SiO_2@TiO_2(B) nanocomposites have a distinct structure, the potential for fast charging, safety in use, and good stability, indicating their use as promising and effective anode materials in better power batteries for the next-generation applications.

1. INTRODUCTION

The demand for implementing innovative technical advances is great at the moment since people desire a safe and comfortable lifestyle. Many smart technology applications, such as intelligent electric cars, portable gadgets, power tools, medical equipment, and communication tools, are now being integrated into daily life. These applications need some source of energy storage in order to operate the electronic system, especially lithium-ion batteries (LIBs).[1] LIBs offer several benefits over conventional batteries, including high energy density, high specific capacity, extended life cycle, no memory effect, long shelf lifetime, and low self-discharge rate.[2,3] LIBs are frequently used as the primary energy storage in a wide range of applications because of their exceptional performance. Generally, LIBs are made up of several components such as a cathode, anode, electrolyte, separator membrane, and so forth. Interestingly, graphite is a typical anode material for commercial LIBs. Despite this, it has a low theoretical specific capacity (372 mA h g^{-1}) and a low operating voltage (0.05 V vs Li/Li^+).[4,5] For these reasons, it could result in the formation of lithium dendrites and lead to a short circuit and the risk of a battery explosion.[6] As a reason, industries are now on the lookout for alternative materials to replace graphite.

Recently, many studies focused on titanium dioxide in the form of the bronze phase (TiO_2(B)), as an alternative anode material to address these safety concerns. Even though TiO_2(B) is a remarkable structure with the lowest density (3.73 g cm^{-3}). The open structure of TiO_2(B) provides 1D

Received: October 26, 2021
Accepted: December 21, 2021
Published: December 31, 2021

infinite channels, which can accommodate the volume changes.[7−9] It also has pseudocapacitive characteristics, which allows for fast lithium storage and transfer during the insertion/extraction operations in LIBs.[10,11] TiO_2(B), a lithium intercalation material, on the other hand, has a low specific capacity (335 mA h g^{-1}) and poor electrical conductivity.[12] These weaknesses could be addressed by merging it with other materials having a higher specific capacity. Silica (SiO_2) is one of the most attractive materials in this decade. It is notable for having a high theoretical specific capacity material (1961 mA h g^{-1}).[13] Silicon (Si) is a naturally abundant element that is primarily found in the form of SiO_2. Furthermore, there have been several instances of extracted SiO_2 from other sources, particularly agricultural byproducts, that is, rice husk,[14] bamboo leaf,[15] corn cob,[16] and sugarcane bagasse.[17] Therefore, natural SiO_2, especially rice husk-derived SiO_2 (Rh-SiO_2), was effectively composited with other anodes to overcome the low specific capacity and environmental issue. Nonetheless, the major drawback of SiO_2 is low conductivity, which makes it difficult for it to be used in batteries.[18] This issue of SiO_2 can be mitigated by augmenting it with another alternative anode material to enhance electron transportation along the electrode, especially tin (Sn). Because of its high conductivity and theoretical specific capacity (994 mA h g^{-1}), Sn is an impressive material for anode application due to its high theoretical capacity and conductivity.[19] However, Li−Sn intermetals are brittle and readily pulverized due to significant lithium-driven volume change during charge−discharge processes, resulting in loss of electronic contact between particle−particle and particle−current collectors.[20] This issue, which causes battery failure, has been a key obstacle in commercialization and efforts to address this restriction. The effective ways of reducing the volume change involved electrode cracking alleviation through the creation of less mechanical stress and reducing the particle size of the anode material.[21] As a result, designing nanostructures and fabricating TiO_2(B)-based composites are the primary strategies that aim to improve electrochemical performance and continue to be a challenge.[22,23] The synergistic impact of the extremely stable and fast-Li diffusion TiO_2(B)-based substrate and high-capacity alloying-type anodes (SiO_2), in combination with conductive Sn, offers not only a permeating electron network but also advantages in high capacity. We believe that instead of just simplified physical mixing, the rational design of such heterogeneous nanostructures is key in achieving excellent electrochemical performance.

Herein, the goal of this work is to combine the outstanding benefits of TiO_2(B), SiO_2, and Sn materials through nanocomposite design. Individually, the three components, TiO_2(B), rice husk-derived SiO_2, and Sn, were synthesized using a hydrothermal method followed by a calcination procedure,[24,25] recrystallization,[26] and chemical reduction.[27,28] These approaches are simple, ecologically friendly, and inexpensive. To reveal battery performances, these synthesized nanocomposite materials were fabricated as the electrode for coin cell production, and their electrochemical properties were also evaluated. To summarize, these preparative nanocomposites are intended to have a high specific capacity, quick charge ability, long cycle life, and safety in use, making them a potential anode material for next-generation LIBs.

2. RESULTS AND DISCUSSION

2.1. Sn−SiO_2@TiO_2(B) Characterization. The synthesized products were initially characterized using the X-ray diffraction (XRD) technique to indicate phase formation and crystallinity. Figure 1 illustrates the XRD patterns of TiO_2(B),

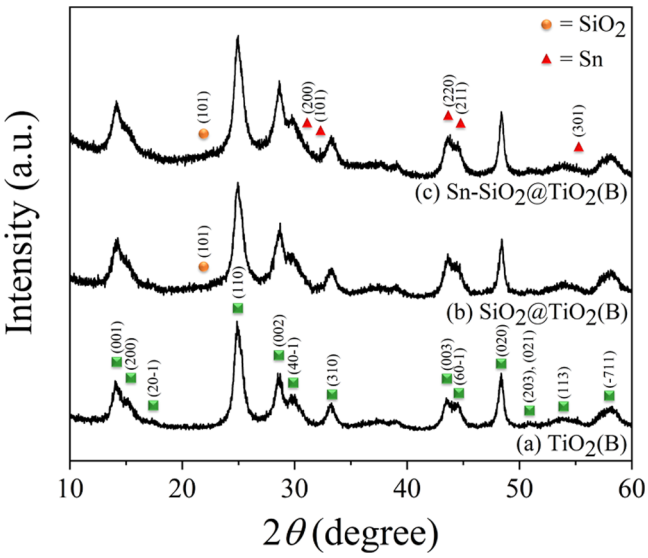

Figure 1. XRD patterns of prepared products: (a) TiO_2(B), (b) SiO_2@TiO_2(B), and (c) Sn−SiO_2@TiO_2(B).

SiO_2@TiO_2(B), and Sn−SiO_2@TiO_2(B) composite products. Given the sharp and high-intensity diffraction peaks in all XRD patterns in Figure 1a, the major diffraction patterns can be effectively indexed as the monoclinic crystalline structure of TiO_2(B) belonging to JCPDS no. 35-0088. These results revealed that the TiO_2(B) phase had a high crystalline structure and suggested a preferential crystallographic orientation of the TiO_2(B) nanorod because the XRD peak, (020) plane, located at approximately $2\theta = 48°$ was abnormally high. Moreover, after carefully considering, a broad peak observed at ∼22° could be attributed well to the overlapping peaks of TiO_2(B) and amorphous SiO_2 in the SiO_2@TiO_2(B) nanocomposite, as displayed in Figure 1b. Remarkably, no crystalline SiO_2 patterns were fully evident in any of the SiO_2-based composite products, owing to the fact that all composites included SiO_2 particles in an amorphous phase, represented as a broad shoulder pattern, and their particle sizes were anticipated to be those of nanoparticles. XRD patterns of the Sn−SiO_2@TiO_2(B) composite following Sn addition to SiO_2@TiO_2(B) are shown in Figure 1c. There were minor diffraction peaks at 2θ of 30.6, 32.0, 43.7, and 44.8°, which corresponded to the Sn metal (JCPDS no. 04-0673). Nonetheless, all these peaks were found to be low in intensity when compared to TiO_2(B) peaks since the quantity of Sn in this composite was relatively low. Furthermore, Sn particle sizes were estimated to be in the nanoscale range, which influenced the broad- and low-intensity diffraction peaks. To validate the presence of SiO_2 and/or Sn, these products should indeed be investigated further using additional methods, scanning electron microscopy (SEM)−energy X-ray dispersive system (EDS), transmission electron microscopy (TEM)−selected area electron diffraction (SAED), and HR-TEM as discussed in the following sections.

https://doi.org/10.1021/acsomega.1c05982
ACS Omega 2022, 7, 1357−1367

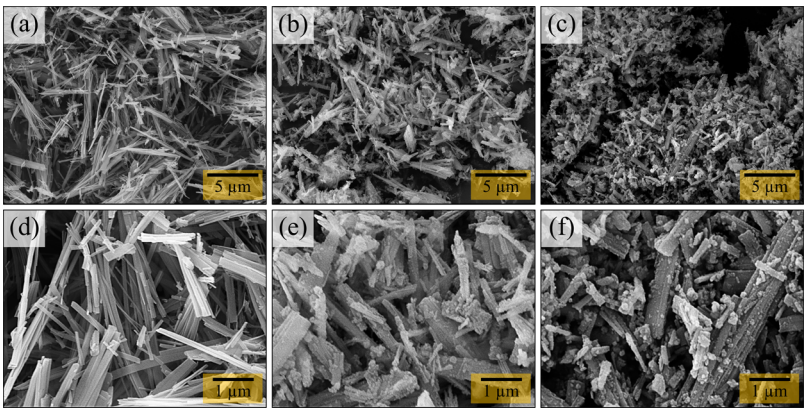

Figure 2. SEM images of the prepared products: (a) TiO_2(B), (b) SiO_2@TiO_2(B), and (c) Sn−SiO_2@TiO_2(B) and their higher magnification views: (d) TiO_2(B), (e) SiO_2@TiO_2(B), and (f) Sn−SiO_2@TiO_2(B).

SEM was used to investigate the morphology of the synthesized products, TiO_2(B), SiO_2@TiO_2(B), and Sn−SiO_2@TiO_2(B). The morphological features and topography of TiO_2(B), SiO_2@TiO_2(B), and Sn−SiO_2@TiO_2(B) samples in the low-magnification (5000×) and close-up views (20,000×) are shown in Figure 2. TiO_2(B), as shown in Figure 2a, has an elongated rod-like shape. A higher magnification image of TiO_2(B) nanorods is displayed in Figure 2d, which appeared in various sizes and lengths in the range of 0.2−5 μm. Small spherical particles adhere homogenously to TiO_2(B) nanorods in SiO_2@TiO_2(B), as shown in Figure 2b,e. As a consequence of co-precipitation between TiO_2(B) rods and recrystallized SiO_2, these small particles deposited on nanorods were anticipated as SiO_2. The SEM images of Sn−SiO_2@TiO_2(B) differ slightly from those of SiO_2@TiO_2(B), as shown in Figure 2c,f. The number of small particles increased significantly when compared to the SiO_2@TiO_2(B) sample, due to the addition of Sn in the SiO_2@TiO_2(B) nanocomposite. Although the SEM technique can show relatively small spherical particles on TiO_2(B) nanorods, the SiO_2 and Sn particles in the composites cannot be distinguished. Therefore, the EDS method was used to validate the existence of SiO_2 and Sn in the prepared nanocomposites. WDS analysis was utilized to examine the proportion of weight and atoms of elements to validate the existence of TiO_2(B), SiO_2, and Sn in the preparative Sn−SiO_2@TiO_2(B) nanocomposite, as shown in Table 1. The

Table 1. Quantitative Elemental Analysis of the Prepared Product Using the WDS Method

	Sn−SiO_2@TiO_2(B)					
elements	weight %	SD (wt %)	RSD (%)	atom %	SD (at %)	RSD (%)
Ti K	41.550	1.017	13.535	21.658	4.867	22.472
Si K	3.235	0.312	9.645	2.854	0.395	13.845
Sn L	6.831	1.017	14.884	1.437	0.332	23.074
O K	48.385	6.651	13.746	74.051	5.483	7.405

WDS results indicated that the Ti K, Si K, Sn L, and O K elements' signals were obviously found in Sn−SiO_2@TiO_2(B) with a weight percentage of 41.550, 3.235, 6.831, and 48.385, respectively. The tiny spherical particles on the TiO_2(B) rods probably represent SiO_2, while the Sn element was discovered in Sn−SiO_2@TiO_2(B) samples, as displayed in the scanning TEM (STEM)−EDS mapping images (Figure S1). As a result, Sn particles could be well considered to be distributed on TiO_2(B) nanorods together with SiO_2 nanoparticles. As shown in Table 2, the weight percentages of Ti, Si, and Sn elements in

Table 2. Calculated Weight Percent of the Phase and Calculated Theoretical Specific Capacity of the Prepared Product

	Sn−SiO_2@TiO_2(B)		
phase composition	TiO_2(B)	SiO_2	Sn
theoretical specific capacity (mA h g^{-1})	335	1965	993
calculated wt % of obtained phases (wt %)	83.45	8.33	8.22
calculated theoretical specific capacity (mA h g^{-1})	524.86		

WDS analysis were employed to calculate the weight percent to estimate the phase composition in all prepared nanocomposites, as shown in Table 2. As a consequence, the theoretical specific capacities of Sn−SiO_2@TiO_2(B) products were calculated based on WDS measurement to be 524.86 mA h g^{-1}. These calculated theoretical specific capacities will indeed be evaluated with experimental specific capacities, as addressed in the section on electrochemical performance. WDS has significant advantages in terms of the peak-to-background ratio, greater elemental sensitivity, and superior energy resolution of characteristic X-ray peaks to eliminate peak overlaps. As a result, the WDS technique, which corresponds to the STEM−EDS technique, can determine the precise quantity of acquired element signals in a Sn−SiO_2@TiO_2(B) sample.

Up to this point, XRD and SEM techniques have been used to identify the structure of the synthesized products. To consolidate further insights into the microstructures of the prepared products, the TEM technique was used. The TEM image in Figure 3a shows the morphology of TiO_2(B) to be a rod-like structure with a diameter in the range of 100−250 nm. Also, the SAED pattern in Figure 3d taken from the TiO_2 rod in Figure 3a shows he [020] rod growth direction, corresponding to the preferred orientation of the [020] direction in the XRD results. Besides, this characteristic promotes fast lithium diffusion along with the structure.[29−31] Figure 3b shows TEM images of the SiO_2@TiO_2(B) product. It is obvious that the SiO_2 particles were thoroughly deposited on the TiO_2(B) rods. Furthermore, the distributed SiO_2 particles, having a diameter of approximately 10 nm, were consistent with those observed in the SEM images. The TEM

https://doi.org/10.1021/acsomega.1c05982
ACS Omega 2022, 7, 1357−1367

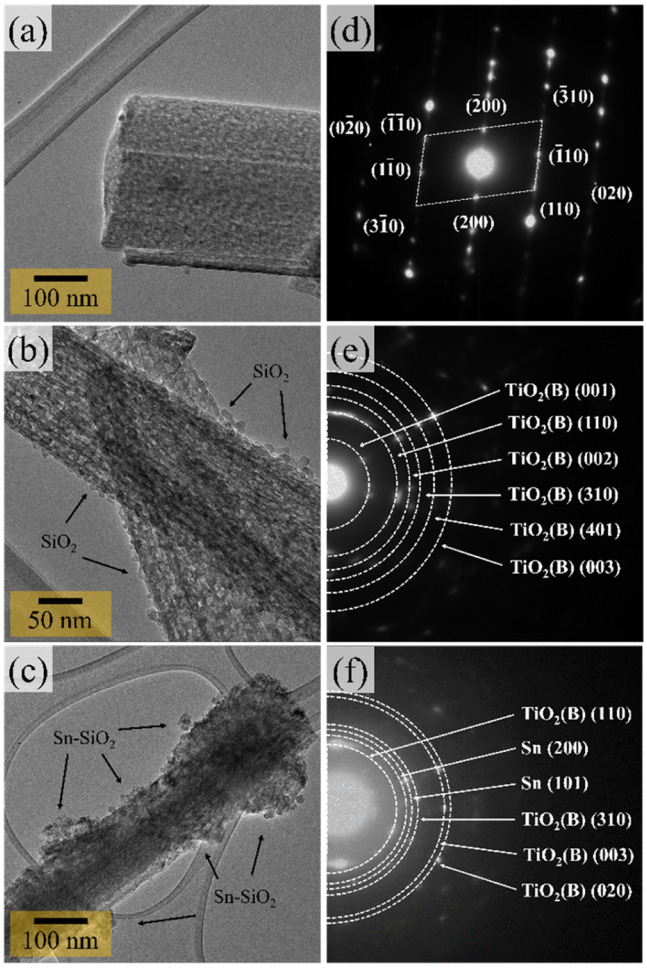

Figure 3. TEM images of prepared products: (a) TiO_2(B), (b) SiO_2@TiO_2(B), and (c) Sn−SiO_2@TiO_2(B) and SAED pattern insets: (d) TiO_2(B), (e) SiO_2@TiO_2(B), and (f) Sn−SiO_2@TiO_2(B) nanocomposites.

image of the Sn−SiO_2@TiO_2(B) product is shown in Figure 3c. The tiny spherical particles and agglomerated particles of Sn were found to be attached to SiO_2@TiO_2(B) nanorods. It cannot, however, be analyzed to recognize individual SiO_2 and Sn nanoparticles. As this reason, the SAED pattern observations were employed to confirm phase components in different products, as illustrated in Figure 3d−f. In the instance of TiO_2(B), the SAED pattern from a single nanorod, displayed in the inset of Figure 3d, demonstrates a set of spot diffraction patterns matching a completely single crystal of the TiO_2(B) phase. Importantly, the spot diffraction patterns from nanorods revealed a growth direction along [020], which corresponded to the preferred [020] orientation correlated in XRD patterns. This appears to be the gist of the small porous channel's insights. It is well-known that this is caused by the open structures in the TiO_2(B) nanorod that provide one-dimensional infinite channels related to this direction.[32] Due to its nanosized range and amorphous character, the diffraction patterns of SiO_2 did not appear, as displayed in Figure 3e. On the other hand, the ring diffraction patterns in Figure 3f could be indexed as Sn and TiO_2(B) phases. It can confirm the presence of Sn in the Sn−SiO_2@TiO_2(B) nanocomposite.

The HR-TEM image of the Sn−SiO_2@TiO_2(B) nanocomposite was captured near the edge of the nanorod, as seen in the low-magnification TEM image in Figure 4 (yellow

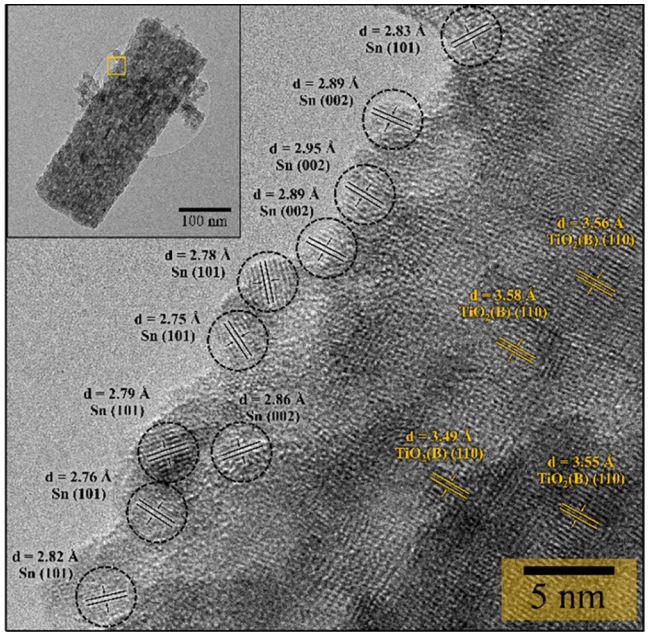

Figure 4. HR-TEM images with the lattice fringes of Sn−SiO_2@TiO_2(B) and the low-magnification TEM image inset.

square). The lattice patterns of the nanoparticles and nanorod were observable, indicating that these nanoparticles and nanorod were crystalline. The nanoparticles had lattice spacings of approximately d = 2.92 and 2.79 Å for the (200) and (101) planes of the Sn phase, respectively. The average crystalline size of Sn on the surface of a nanorod is around 5 nm. Also, the HR-TEM image definitely demonstrates that the distance between the lattice fringes (d = 3.56 Å) in the aligned nanorods could be ascribed to the interplanar distance of the TiO_2 bronze-phase (110) plane, which agreed with XRD results. Unfortunately, the SiO_2 lattice fringe was not observed, which verified the low-crystalline character of the SiO_2 nanoparticles. According to the matching lattice fringes, the nanoparticles are polycrystalline Sn structures, whereas the aligned nanorods are single-crystalline TiO_2(B) structures, which are consistent with the SAED patterns and XRD results.

From the abovementioned results, the unique nanostructures were successfully produced based on the characterization of synthesized TiO_2 (B), SiO_2@TiO_2(B), and Sn−SiO_2@TiO_2 nanocomposites, and the remarkable properties of these nanocomposite materials can be used as anodes for lithium-ion batteries. The schematic diagram, as shown in Figure 5, was utilized to explain the reaction mechanism of the unique nanostructural Sn−SiO_2@TiO_2 nanocomposite formation: First, a hydrothermal method followed by calcination was used to prepare TiO_2(B) nanorods. The prepared TiO_2(B) nanorods were then homogeneously distributed in the Na_2SiO_3 solution, which was prepared from rice husk SiO_2 and NaOH. After the pH adjustment, the hydroxyl groups of both TiO_2(B) and nano-SiO_2 were attached by hydrogen bonds (−Si−O−H···O−Ti− and −Si−O···H−O−Ti−).[33] At this stage, therefore, the chemical combination between SiO_2 nanospheres and nano-TiO_2 nanorods was formed by the interaction of hydroxyl groups on their surfaces. Then, the water released by the dehydroxylation of the interfaces was further removed during the drying process to form the SiO_2@TiO_2(B) nanocomposite.[34] The formation of the SiO_2@TiO_2(B) nanocomposite was confirmed with the XRD,

https://doi.org/10.1021/acsomega.1c05982
ACS Omega 2022, 7, 1357−1367

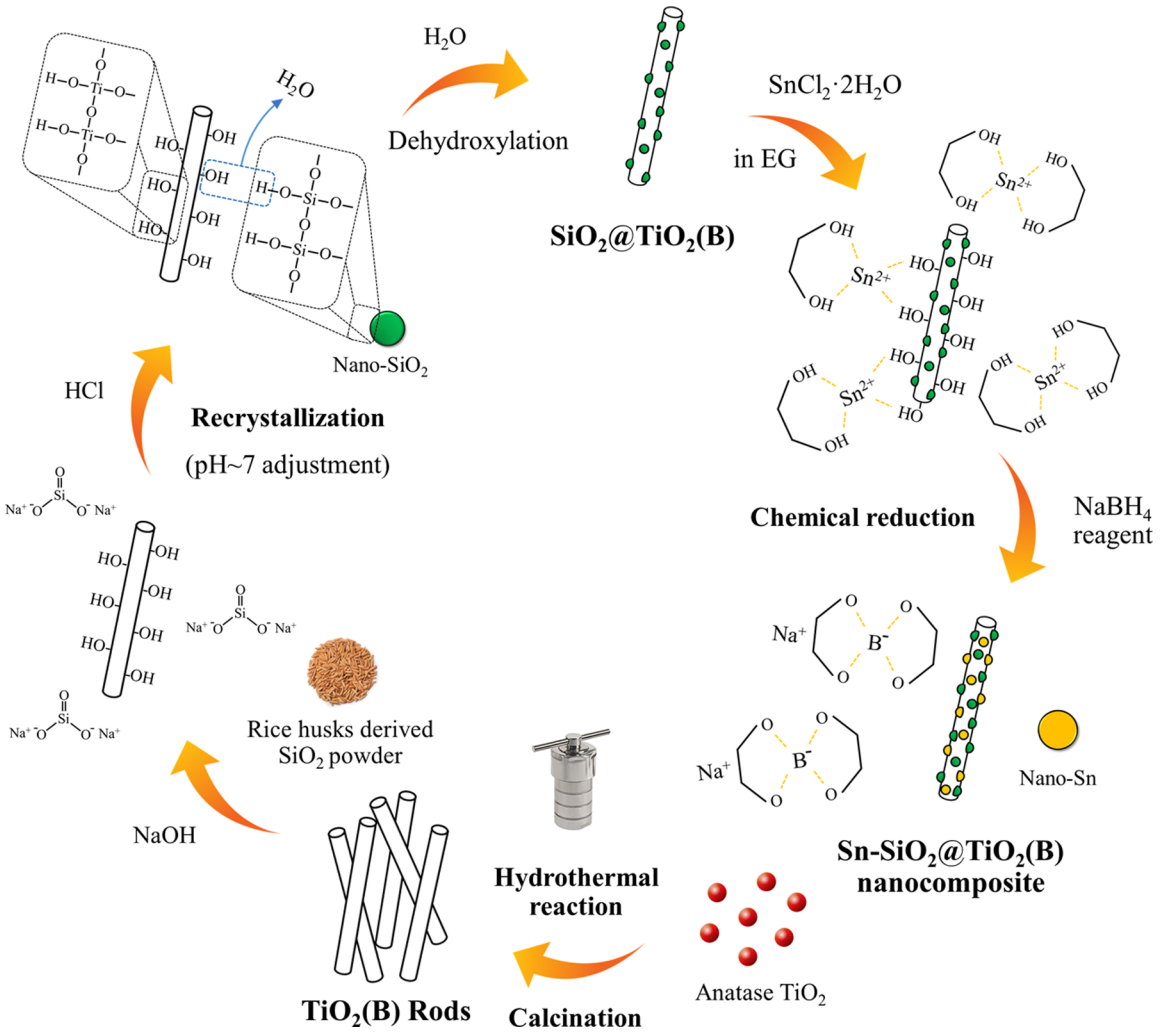

Figure 5. Schematic illustration of the synthesis routes of the Sn−SiO_2@TiO_2(B) nanocomposite.

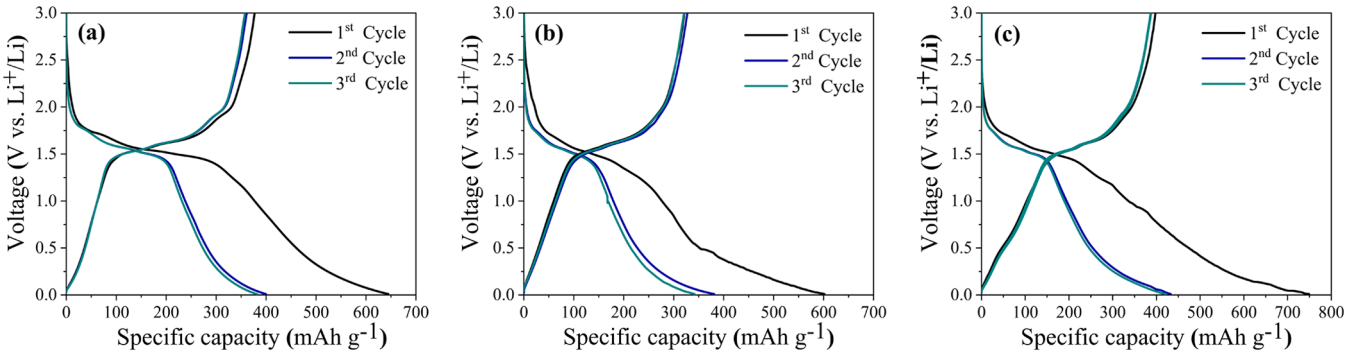

Figure 6. GCD profiles at the first three cycles of (a) TiO_2(B), (b) SiO_2@TiO_2(B), and (c) Sn−SiO_2@TiO_2(B) nanocomposites at a current density of 50 mA g^{-1}.

TEM, and STEM−EDS (Figure S1) techniques, which will be discussed later. At this point, the nano-SiO_2 was driven to encounter the TiO_2(B)-surface directly, enhancing the probability of intercontact and reaction. It is suspected that this is due to self-condensation between the reactive hydroxyl groups on both surfaces, resulting in the creation of a coupled bond (−Ti−O−Si−) stronger than van der Waals forces and other physical forces.[35] As a result, chemical and physical interactions are critical for a durable chemical connection. The bonding mechanism of the SiO_2@TiO_2(B) nanocomposite in this work was similar to that in the previous reports of the SiO_2−TiO_2 composite formation.[33,34,36] Therefore, it was possible to confirm that the SiO_2@TiO_2 composite was successfully synthesized. The produced SiO_2@TiO_2(B) was then transferred to a solution of $SnCl_2·2H_2O$ to load Sn on the SiO_2@TiO_2(B) through chemical reduction, where $NaBH_4$ was employed as a reducing agent. The Sn^{2+} in ethylene glycol solvent was in the form of ionic liquid (Sn^{2+}•2[HO−CH_2CH_2−OH]), which also acts as a stabilizing agent.[37] Then, they were immobilized on the surface of both TiO_2(B)

https://doi.org/10.1021/acsomega.1c05982
ACS Omega 2022, 7, 1357−1367

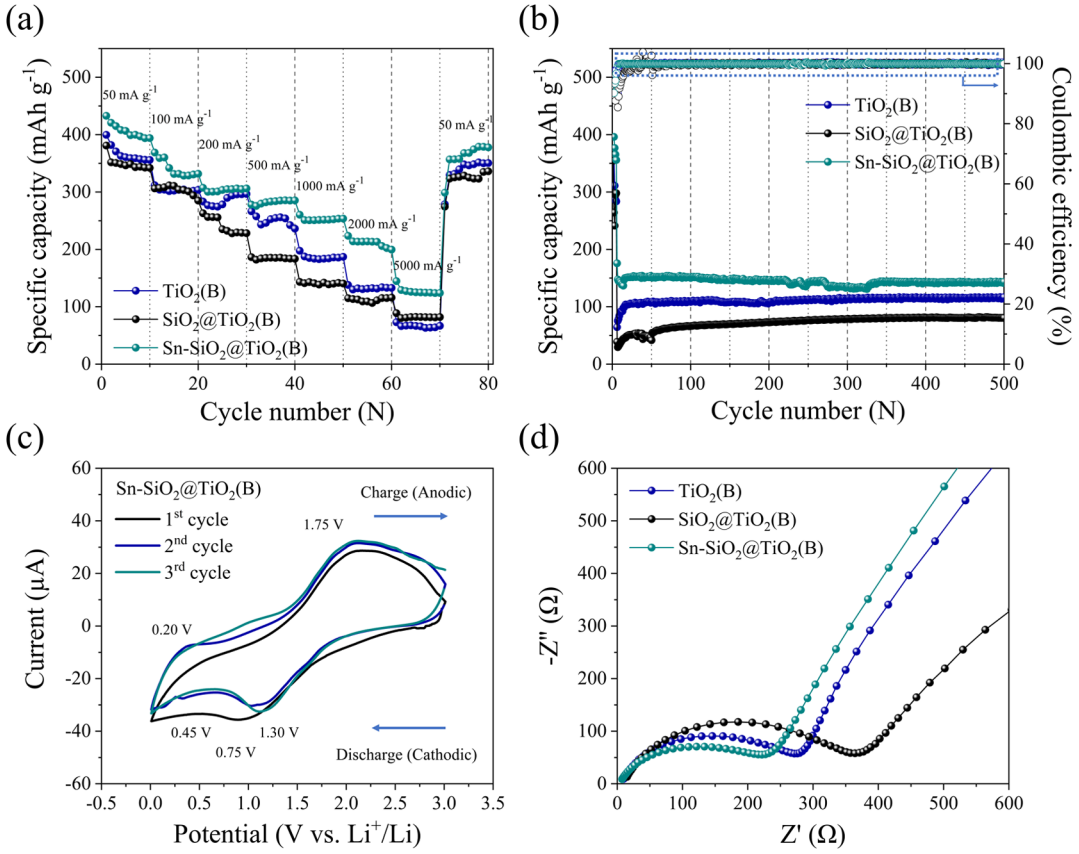

Figure 7. Electrochemical performance of as-prepared (a) TiO_2(B), (b) SiO_2@TiO_2(B), and (c) Sn−SiO_2@TiO_2(B), (a) rate cycle capability at different current densities in the range of 50−5000 mA g^{-1}, (b) long-term cycle stability and the corresponding Coulombic efficiency at a fast-charging state of 5000 mA g^{-1} for 500 cycles, (c) CV curves of first-three cycles of the Sn−SiO_2@TiO_2 electrode between 0.01 and 3.0 V at a scan rate of 0.2 mV s^{-1}, and (d) Nyquist plots of as-prepared electrodes.

and SiO_2 via dipole−dipole interaction forces and then formed Sn nanoparticles after reduction reaction. However, there were some particle agglomerations because of the high surface energy of nanoparticles. The total surface energy of the system is increasing. Therefore, the nanoparticles should coagulate and form large ones to reduce the total surface energy of the system, as can be seen in the TEM images. Finally, the Sn−SiO_2@TiO_2(B) nanocomposite successfully produced as one-of-a-kind nanostructure with Sn and SiO_2 nanoparticles assembled on TiO_2(B) nanorods.

2.2. Electrochemical Performance. To examine the electrochemical performance, the as-prepared TiO_2(B), SiO_2@TiO_2(B), and Sn−SiO_2@TiO_2(B) electrodes were produced and then fabricated into coin battery cells. The galvanostatic charge−discharge (GCD) profiles of all electrodes were well investigated in the half-cells, as shown in Figure 6a−c, which were measured during the first three cycles at the same current density of 50 mA g^{-1} in the potential range of 0.01−3.00 V (vs Li^+/Li). The initial discharge capacity of the prepared electrodes was discovered to be 644.77 mA h g^{-1} for bare TiO_2 (B), 601.57 mA h g^{-1} for SiO_2@TiO_2(B), and 749.26 mA h g^{-1} for Sn−SiO_2@TiO_2(B), which were greater than the calculated theoretical capacity. However, the irreversibility during the initial discharge stage comes as no surprise.[38,39] The first charge capacity of TiO_2 (B), SiO_2@TiO_2(B), and Sn−SiO_2@TiO_2(B) electrodes was rapidly reduced to 377.02, 321.30, and 397.87 mA h g^{-1}, corresponding to the initial Coulombic efficiency (ICE) of 58.47, 53.41, and 53.10%, respectively. When compared to bare TiO_2(B), the ICE values of both SiO_2@TiO_2(B) and Sn−SiO_2@TiO_2(B) electrodes were relatively low, which associated with the irreversible formation of Li_2O and lithium silicates at the first cycle. Also, SiO_2 acted as an insulator with low intrinsic electrical conductivity, which was the cause of the low initial Coulombic efficiency.[40] The increased specific capacity and ICE of Sn−SiO_2@TiO_2(B) were attributed to the fact that the presence of Sn improved the overall electrical conductivity of the Sn−SiO_2@TiO_2(B) electrode, allowing electrons to arrive at the surface of TiO_2(B) and SiO_2, facilitating Li^+ transfer in the nanocomposites.[41] Furthermore, the advantages of nanostructured Sn provide a high surface area and a short lithium-ion diffusion path length, which offer a high contact area with the electrolyte and a large active site for lithium storage. For these reasons, adding Sn, the Sn−SiO_2@TiO_2(B) electrode, can effectively improve its electrochemical activity and specific capacity. The discharge capacity of prepared TiO_2 (B), SiO_2@TiO_2(B), and Sn−SiO_2@TiO_2(B) electrodes in the second cycle was 399.69, 381.00, and 432.83 mA h g^{-1}, respectively, which was lower than that in the first cycle. However, the ICE was recovered to be 90.37, 85.90, and 89.36%, respectively. These may be attributed to the reducing effect of SEI film formation in the second cycle and the fact that their unique nanostructure can function well as an excellent anode, leading to an almost completely reversible reaction of Li^+.

https://doi.org/10.1021/acsomega.1c05982
ACS Omega 2022, 7, 1357−1367

Figure 7a shows the rate capability of the prepared electrodes at different current densities ranging from 50 to 5000 mA h g^{-1}, reflecting the interdependent impacts of three prepared nanocomposite anodes that are appropriate for individual applications. It is evident that the discharge specific capacity of prepared electrodes at each current rate exhibited comparatively good capacity retention. At a fast-charge state of 5000 mA g^{-1}, the Sn−SiO_2@TiO_2(B) electrode achieved the greatest specific capacity of approximately 140 mA h g^{-1}. The specific capacity was then quickly raised to 400 mA h g^{-1} without loss of capacity when the current rate was returned to the starting rate of 50 mA g^{-1}, indicating outstanding rate capability and outstanding cycle performance. Thus, the existence of a pseudo-capacitive channel in TiO_2(B), which parallels to its layered perovskite structure, allows the possibility of fast Li-ion diffusion pathways across the structure of TiO_2(B)-based nanocomposite electrodes.[42]

For the long-term cycle test, the measurements were carried out at an activating current density of 100 mA g^{-1} for 10 cycles and then directly at a fast-charging current density of 5000 mA g^{-1} until 500 cycles to evaluate the cycle stability of the electrode materials. The results are shown in Figure 7b. After the activating stage, the discharge capacitances of the three prepared electrodes achieve stable values. The discharge capacitance values of the three prepared electrodes reach steady levels after 10 cycles. After 500 cycles, the specific capacities of the TiO_2(B), SiO_2@TiO_2(B), and Sn−SiO_2@TiO_2(B) electrodes were 115.14, 81.39, and 143.03 mA h g^{-1}, respectively. Evidently, Sn nanoparticles can enhance the specific capacity of nanorod-TiO_2(B), making it suitable for prolonged cycle stability at high current density. Importantly, the Sn−SiO_2@TiO_2(B) structure was unique because it can overcome the expansion−contraction phenomenon driven by charge−discharge operations, which causes electrode cracking after many cycles. As a result, the fading capacity was not observed during several cycles. Notably, Sn−SiO_2@TiO_2(B) demonstrated not only exceptional high rate capability but also excellent cycle stability.

Figure 7c shows the first three CV curves of the Sn−SiO_2@TiO_2(B) electrode in a voltage window of 0.01−3.00 V versus Li/Li^+ at a scan rate of 0.2 mV s^{-1}. In the CV curves, there appeared to be a cathodic peak at 0.75 V, which occurs only in the first cycle and is therefore ascribed to electrolyte decomposition for the formation of the solid−electrolyte interphase (SEI) layer.[43] Furthermore, there were significant reduction peaks between 0.45 and 1.00 V in the first cycle. Thus, amorphous SiO_2 was reduced to form Si and Li_2O in a discharge state at approximately 0.45 V, which agreed to eq 1.[44,45] The peak at 1.00 V suggests a chemical interaction between SiO_2 and Li^+. As demonstrated in eqs 2 and 3, when the material was first discharged, amorphous SiO_2 was converted to Si and produced $Li_2Si_2O_5$ or Li_4SiO_4.[46,47] The irreversible Li_4SiO_4 phase produced during the reaction required a significant capacity. As indicated in eq 4, the characteristic peaks associated with the reversible alloy/de-alloy reaction with Li^+ of Si include cathodic peaks of 0.19−0.21 V, which correspond to the transformation from Si to Li_xSi, and anodic peaks of 0.52 V (Li_xSi to Si).[48] Therefore, this reaction contributes to the electrode's lithium storage capacity. In the second and third cycles, the CV curves become stable over the following scan cycles, reflecting the equivalent reversible behavior. The discharge reaction responses could be well classified as follows

$$SiO_2 + 4Li^+ + 4e^- \rightarrow 2Li_2O + Si \quad (1)$$

$$5SiO_2 + 4Li^+ + 4e^- \leftrightarrow 2Li_2Si_2O_5 + Si \quad (2)$$

$$2SiO_2 + 4Li^+ + 4e^- \rightarrow Li_4SiO_4 + Si \quad (3)$$

$$Si + xLi^+ + xe^- \leftrightarrow Li_xSi \qquad (0 \le x \le 4.4) \quad (4)$$

This phenomenon could be well attributed to the fact that TiO_2 nanorods have freely accessible parallel channels that follow the [001] direction and therefore can have intercalated/deintercalated lithium ions without causing severe structural deformation.[49] The CV curves reveal a couple of peaks with potentials in the 1.3/1.75 V range, which have all been attributed to oxidation/reduction of the Ti^{3+}/Ti^{4+} coupling in TiO_2(B).[11] This is a characteristic pseudocapacitive behavior of lithium storage in TiO_2(B). Furthermore, the Li-ion diffusion process into TiO_2(B) was effectively encouraged to transport the Li-ion along with the structure, as indicated in eq 5.[50]

$$xLi^+ + xe^- + TiO_2(B) \leftrightarrow Li_xTiO_2(B) \qquad (0 \le x \le 1) \quad (5)$$

While the process in eq 6 occurred in the formation of a Li_xSn alloy and dealloying, it is indeed reversible. A series of Li−Sn alloys, in the form of Li_2Sn_5, LiSn, Li_7Sn_3, Li_5Sn_2, $Li_{13}Sn_5$, Li_7Sn_2, and $Li_{22}Sn_5$, were formed at potentials ranging from 0.01 to 0.60 V.[51] Based on the alloy process, up to 4.4 Li atoms can be stored per Sn atom ($Li_{22}Sn_5$), resulting in a maximum theoretical capacity.[52]

$$Sn + xLi^+ + xe^- \leftrightarrow Li_xSn \qquad (0 \le x \le 4.4) \quad (6)$$

To study the structural and interfacial behavior of as-prepared nanocomposite electrodes further, electrical impedance spectroscopy (EIS) was performed at room temperature across a frequency range of 100 kHz−0.1 Hz. Nyquist plots of TiO_2(B), SiO_2@TiO_2(B), and Sn−SiO_2@TiO_2(B) electrodes can be seen in Figure 7d. The semicircle at high-to-medium frequency corresponded to the charge-transfer resistance (R_{ct}) and double-layer capacitance through the electrode−electrolyte interface, whereas the inclined line at low frequency corresponds to the Warburg diffusion impedance (Z_w) and also to the diffusion resistance of lithium ions through the solid-state electrodes described earlier in this section.[53,54] The R_{ct} values of the fabricated electrode were incremented in the following order: Sn−SiO_2@TiO_2(B) (~250 Ω) < TiO_2(B) (~300 Ω) < SiO_2@TiO_2(B) (~400 Ω). Obviously, the R_{ct} of the SiO_2@TiO_2 electrode is lower than that of the TiO_2(B) and Sn−SiO_2@TiO_2(B) electrodes, demonstrating that amorphous SiO_2 nanoparticles could decrease electrical conductivity. The semicircle at a high-to-medium frequency of prepared electrodes revealed that interfacial impedance was reduced when Sn was added, implying that Sn nanoparticles were consistently deposited to serve the conductivity.[55] This characteristic could potentially improve electrical contraction, resulting in lower internal resistance and better Li-ion transportation in the composited electrode. Importantly, the pseudocapacitive channel in TiO_2(B), according to theory, could improve the faster Li-ion diffusion. It implied that the Sn−SiO_2@TiO_2(B) electrode performs better than the other electrodes in terms of reducing interfacial impedance.

In summary, this study discovered combining Sn, SiO_2, and TiO_2(B) through a nanocomposite, which incorporated

https://doi.org/10.1021/acsomega.1c05982
ACS Omega 2022, 7, 1357−1367

innovatively well together to minimize the overall cell resistance, enhance lithiation/de-lithiation kinetics, produce a low cost, be environmentally friendly, have good safety, and exhibit significantly increased specific capacity with excellent cycle stability, resulting in excellent performance of the Sn−SiO_2@TiO_2(B) composite electrode. Our research claims that under the fast-charging stage, their specific capacities, rate capabilities, and cyclic stability are higher than those TiO_2(B)-based anode materials studied previously, TiO_2(B) nanowire,[56] TiO_2(B) nanotube,[57] nitrogen-doped TiO_2(B),[58] zirconium-doped TiO_2(B),[59] TiO_2(B)/anatase,[60,61] TiO_2(B)/graphene,[62−64] and TiO_2(B)/SnO_2,[49] TiO_2(B)/carbon.[65] Finally, the new structural design of Sn−SiO_2@TiO_2(B) nanocomposites has one of the greatest battery performances and is one of the most promising fast-charging anode materials for next-generation lithium-ion batteries.

3. CONCLUSIONS

The innovative nanocomposites designed with Sn−SiO_2@TiO_2(B) were effectively prepared in this study using a simple chemical approach. Rice husk-derived SiO_2 and Sn nanoparticles attached evenly on the surface of TiO_2(B) nanorods. Individual SiO_2 and Sn particles ranged in size from 5 to 10 nm, with excellent distribution. When compared to other products, the Sn−SiO_2@TiO_2(B) electrode exhibited excellent electrochemical characteristics for lithium-ion batteries. The specific capacity with cycle stability of Sn−SiO_2@TiO_2(B), delivering 143.03 mA h g^{-1}, was significantly higher than that of synthesized TiO_2(B)-based products, as was the low internal resistance (∼250 Ω). Importantly, the influence mechanism of SiO_2 and Sn nanoparticles self-assembled on TiO_2(B) to enhance battery performance was thoroughly defined based on the characterization. This research contributed to the improvement of the electrochemical characteristics of TiO_2(B)-based anode materials. As a result, Sn−SiO_2@TiO_2(B) nanocomposites may become the new go-to materials for fast-charging anodes in lithium-ion batteries in the future.

4. EXPERIMENTAL PROCEDURES

4.1. Sn−SiO_2@TiO_2(B) Nanocomposite Preparation. First, TiO_2(B) was produced by dispersing anatase TiO_2 (99%, Ajax Finechem) in a NaOH solution. The suspension was then loaded into a hydrothermal reactor and maintained for 48 h at a hydrothermal temperature of 180 °C. The hydrothermal product was then immersed in a nitric acid solution for 12 h. The acid-treated product was then rinsed with DI water before being dried in an oven. Furthermore, the dried product was heated up to 400 °C for 5 h to produce TiO_2(B). Second, 10% wt SiO_2 was uniformly assembled on the prepared TiO_2(B), as it approached: Acid treatment and calcination were used to extract Rh-SiO_2 powder from rice husks. Rh-SiO_2 then was then subjected to a recrystallization process to purify and minimize particle size. The Rh-SiO_2 was refluxed in a NaOH solution. The refluxed solution was then filtered before being homogeneously blended with TiO_2(B). The pH of the produced combinations was adjusted to a value of 7. To create the SiO_2@TiO_2(B) nanocomposite, the precipitate was collected and washed with DI water. Finally, the prepared SiO_2@TiO_2(B) was composited with Sn utilizing the following chemical reduction procedure: tin(II) chloride dehydrate (98%, Sigma-Aldrich) was dissolved in ethylene glycol (99.9%, J.T. Baker). After that, the SiO_2@TiO_2(B) was submerged in the mixture for 2 h using ultrasonication. After that, the cold and fresh sodium borohydride (98.0%, Sigma-Aldrich) in ethylene glycol, as a reducing agent, was slowly dropped into the mixture under continuous stirring. To eliminate any excess ethylene glycol, the suspension was collected via centrifugation and then washed with ethanol. The obtained product was then dried at 60 °C to produce the Sn−SiO_2@TiO_2(B) nanocomposite.

4.2. Material Characterization. Phase identification of crystalline materials was investigated using the XRD technique (Panalytical). SEM (JEOL JSM-IT800) was used to characterize the morphology and microstructure change of materials. The WDS analyses of the samples were performed to investigate element composition using a JEOL JSM-IT300 scanning electron microscope with an automatic Oxford Instruments Wave detector system using a PET crystal (Si, Sn, Ti) and LSM60 crystal (O). STEM measurements were taken with a JEOL JSM-IT800 scanning electron microscope equipped with an EDS detector to observe the distribution. A transmission electron microscope for obtaining SAED, and a high-resolution view (TEM−SAED and HR-TEM, JEOL JEM-2010) was used to study the morphology and phase formation of as-prepared nanocomposite materials.

4.3. Electrochemical Measurement. Electrochemical experiments were carried out using coin-type cells (CR2016). In the electrode preparation, active materials, conductive Super-P (NCM HERSBIT Chemical Co. Ltd), and sodium alginate (SA) binder (Sigma-Aldrich) in aqueous solution were homogeneously mixed with a weight ratio of 70:15:15. The homogeneous slurry was then coated onto a copper foil using a doctor blade technique. In the coin-cell fabrication, a lithium chip was used as the counter electrode, whereas a Celgard 2400 is employed as the separator. Lithium hexafluorophosphate ($LiPF_6$) solution (Sigma-Aldrich) in ethylene carbonate/dimethyl carbonate (EC)/(DMC) (1:1 by vol %) + 10% fluoroethylene carbonate (FEC) was used as the electrolyte in this study. To study the electrochemical properties of the prepared electrode, the GCD profiles (CG-DG), rate capability, and cycle stability of the as-prepared electrode were evaluated using a battery test system (Neware BTS-4000). Cyclic voltammetry (CV) and EIS were measured using a potentiostat/galvanostat (Autolab PGSTAT302N) at room temperature.

■ ASSOCIATED CONTENT

Supporting Information

The Supporting Information is available free of charge at https://pubs.acs.org/doi/10.1021/acsomega.1c05982.

STEM image (dark field) and STEM-EDS element mapping of Ti, Si, C, O, and Sn in the prepared Sn−SiO_2@TiO_2(B) nanocomposite (PDF)

■ AUTHOR INFORMATION

Corresponding Author

Thapanee Sarakonsri − *Department of Chemistry, Faculty of Science, Chiang Mai University, Chiang Mai 50200, Thailand; Material Science Research Center, Faculty of Science and Center of Excellent for Innovation in Chemistry (PERCH-CIC), Faculty of Science, Chiang Mai University, Chiang Mai 50200, Thailand;* orcid.org/0000-0002-3084-0276; Email: thapanee.s@cmu.ac.th

https://doi.org/10.1021/acsomega.1c05982
ACS Omega 2022, 7, 1357−1367

Authors

Thanapat Autthawong − *Department of Chemistry, Faculty of Science, Chiang Mai University, Chiang Mai 50200, Thailand; Material Science Research Center, Faculty of Science, Chiang Mai University, Chiang Mai 50200, Thailand*

Chawin Yodbunork − *Department of Chemistry, Faculty of Science, Chiang Mai University, Chiang Mai 50200, Thailand; Center of Excellent for Innovation in Chemistry (PERCH-CIC), Faculty of Science, Chiang Mai University, Chiang Mai 50200, Thailand*

Waewwow Yodying − *Department of Chemistry, Faculty of Science, Chiang Mai University, Chiang Mai 50200, Thailand*

Ruttapol Boonprachai − *Department of Chemistry, Faculty of Science, Chiang Mai University, Chiang Mai 50200, Thailand; Material Science Research Center, Faculty of Science, Chiang Mai University, Chiang Mai 50200, Thailand*

Orapim Namsar − *Department of Chemistry, Faculty of Science, Chiang Mai University, Chiang Mai 50200, Thailand*

Ai-shui Yu − *Department of Chemistry, Fudan University, Shanghai 200438, China;* orcid.org/0000-0002-8135-5123

Yothin Chimupala − *Material Science Research Center, Faculty of Science and Department of Industrial Chemistry, Faculty of Science, Chiang Mai University, Chiang Mai 50200, Thailand*

Complete contact information is available at: https://pubs.acs.org/10.1021/acsomega.1c05982

Author Contributions

T.A.: conceptualization, validation, and writing—original draft. C.Y., W.Y., and R.B.: formal analysis, investigation, methodology, and resources. O.N.: validation. A.-s.Y.: visualization. Y.C.: visualization and writing—review and editing. T.S.: supervision and writing—review and editing.

Notes

The authors declare no competing financial interest.

■ ACKNOWLEDGMENTS

This work was supported by the financial funding from the post-doctoral fellowships, Chiang Mai University, Center of Excellence in Materials Science and Technology, and the Program Management Unit for Human Resources and Institutional Development, Postgraduate Education and Research Program in Chemistry (PERCH-CIC), Research and Innovation, Office of National Higher Education Science Research and TSRI, and the Program Management Unit for Human Resources and Institutional Development, Research and Innovation, Office of National Higher Education Science Research and Innovation Policy Council (NXPO) in Global Partnership Project [Grant no. B16F640001]. The authors would also like to thank the Renewable Energy Laboratory-Advanced Battery Research Unit, Department of Chemistry, Chiang Mai University for sample preparation and characterizations. The authors express deep gratitude to Fudan University for their support in coin-battery cell fabrication and electrochemical measurements. Advanced electron microscopy was supported by the Collaborative Research Program of Institute for Chemical Research, Kyoto University [Grant no. 2021-122].

■ REFERENCES

(1) Zhang, W.; Shen, D.; Liu, Z.; Wu, N.-L.; Wei, M. Brookite TiO_2 Mesocrystals with Enhanced Lithium-Ion Intercalation Properties. *Chem. Commun.* **2018**, *54*, 11491−11494.

(2) Madian, M.; Eychmüller, A.; Giebeler, L. Current Advances in TiO_2-Based Nanostructure Electrodes for High Performance Lithium Ion Batteries. *Batteries* **2018**, *4*, 7.

(3) Liu, K.; Liu, Y.; Lin, D.; Pei, A.; Cui, Y. Materials for Lithium-Ion Battery Safety. *Sci. Adv.* **2018**, *4*, 9820.

(4) Kheirabadi, N.; Shafiekhani, A. Graphene/Li-Ion Battery. *J. Appl. Phys.* **2012**, *112*, 124323.

(5) Ncube, N. M.; Zheng, H. The Effect of Synthesis Temperature on the Properties of TiO_2 (B) Nanorods and Its Precursors as Anode Materials for Lithium-Ion Batteries. *Mater. Res. Express* **2020**, *7*, 015504.

(6) Nitta, N.; Wu, F.; Lee, J. T.; Yushin, G. Li-Ion Battery Materials: Present and Future. *Mater. Today* **2015**, *18*, 252−264.

(7) Kim, H.-K.; Mhamane, D.; Kim, M.-S.; Roh, H.-K.; Aravindan, V.; Madhavi, S.; Roh, K. C.; Kim, K.-B. TiO_2-Reduced Graphene Oxide Nanocomposites by Microwave-Assisted Forced Hydrolysis as Excellent Insertion Anode for Li-Ion Battery and Capacitor. *J. Power Sources* **2016**, *327*, 171−177.

(8) Li, Y.; Wang, Z.; Lv, X.-J. N-Doped TiO2 Nanotubes/N-Doped Graphene Nanosheets Composites as High Performance Anode Materials in Lithium-Ion Battery. *J. Mater. Chem. A* **2014**, *2*, 15473−15479.

(9) Chimupala, Y.; Junploy, P.; Hardcastle, T.; Westwood, A.; Scott, A.; Johnson, B.; Brydson, R. Universal Synthesis Method for Mixed Phase TiO_2(B)/Anatase TiO_2 Thin Films on Substrates via a Modified Low Pressure Chemical Vapour Deposition (LPCVD) Route. *J. Mater. Chem. A* **2016**, *4*, 5685−5699.

(10) Opra, D. P.; Gnedenkov, S. V.; Sinebryukhov, S. L. Recent Efforts in Design of TiO_2(B) Anodes for High-Rate Lithium-Ion Batteries: A Review. *J. Power Sources* **2019**, *442*, 227225.

(11) Zukalová, M.; Kalbáč, M.; Kavan, L.; Exnar, I.; Graetzel, M. Pseudocapacitive Lithium Storage in TiO_2(B). *Chem. Mater.* **2005**, *17*, 1248−1255.

(12) Dylla, A. G.; Henkelman, G.; Stevenson, K. J. Lithium Insertion in Nanostructured TiO_2(B) Architectures. *Acc. Chem. Res.* **2013**, *46*, 1104−1112.

(13) Favors, Z.; Wang, W.; Bay, H. H.; George, A.; Ozkan, M.; Ozkan, C. S. Stable Cycling of SiO_2 Nanotubes as High-Performance Anodes for Lithium-Ion Batteries. *Sci. Rep.* **2014**, *4*, 4605.

(14) Cui, J.; Cheng, F.; Lin, J.; Yang, J.; Jiang, K.; Wen, Z.; Sun, J. High Surface Area C/SiO_2 Composites from Rice Husks as a High-Performance Anode for Lithium Ion Batteries. *Powder Technol.* **2017**, *311*, 1−8.

(15) Xu, H.; Zhang, S.; He, W.; Zhang, X.; Yang, G.; Zhang, J.; Shi, X.; Wang, L. SiO_2−Carbon Nanocomposite Anodes with a 3D Interconnected Network and Porous Structure from Bamboo Leaves. *RSC Adv.* **2016**, *6*, 1930−1937.

(16) Chanadee, T. Experimental Studies on Self-Propagating High-Temperature Synthesis of Si-SiC Composite from Reactants of SiO_2 Derived from Corn Cob Ash/C/Mg. *J. Aust. Ceram. Soc.* **2017**, *53*, 245−252.

(17) Norsuraya, S.; Fazlena, H.; Norhasyimi, R. Sugarcane Bagasse as a Renewable Source of Silica to Synthesize Santa Barbara Amorphous-15 (SBA-15). *Procedia Eng.* **2016**, *148*, 839−846.

(18) Jumari, A.; Yudha, C. S.; Widiyandari, H.; Lestari, A. P.; Rosada, R. A.; Santosa, S. P.; Purwanto, A. SiO_2/C Composite as a High Capacity Anode Material of LiNi0.8Co0.15Al0.05O2 Battery Derived from Coal Combustion Fly Ash. *Appl. Sci.* **2020**, *10*, 8428.

(19) Kure-Chu, S.-Z.; Satoh, A.; Miura, S.; Mizuhashi, M.; Yashiro, H. Controllable Fabrication of Nanostructured Sn-TiO_2 Composite Films on Cu Sheets as Anode Materials for Lithium-Ion Battery. *ECS Trans.* **2015**, *64*, 69−80.

(20) Winter, M.; Besenhard, J. O. Electrochemical Lithiation of Tin and Tin-Based Intermetallics and Composites. *Electrochim. Acta* **1999**, *45*, 31−50.
(21) Kamali, A. R.; Fray, D. J. Tin-Based Materials as Advanced Anode Materials for Lithium Ion Batteries: A Review. *Rev. Adv. Mater. Sci.* **2011**, *27*, 14−24.
(22) Demirocak, D. E.; Srinivasan, S. S.; Stefanakos, E. K. A Review on Nanocomposite Materials for Rechargeable Li-Ion Batteries. *Appl. Sci.* **2017**, *7*, 731.
(23) Wang, S.; Yang, Y.; Dong, Y.; Zhang, Z.; Tang, Z. Recent Progress in Ti-Based Nanocomposite Anodes for Lithium Ion Batteries. *J. Adv. Ceram.* **2019**, *8*, 1−18.
(24) Yodying, W.; Autthawong, T.; Chimupala, Y.; Sarakonsri, T. Nanostructural Characterization of Nitrogen-Doped Graphene/Titanium Dioxide (B)/ Silicon Composite Prepared by Dispersion Method. *Solid State Phenom.* **2020**, *302*, 27−35.
(25) Półrolniczak, P.; Walkowiak, M. Titanium Dioxide High Aspect Ratio Nanoparticle Hydrothermal Synthesis Optimization. *Open Chem.* **2015**, *13*, 75−81.
(26) Namsar, O.; Autthawong, T.; Laokawee, V.; Boonprachai, R.; Haruta, M.; Kurata, H.; Yu, A.; Chairuangsri, T.; Sarakonsri, T. Improved Electrochemical Performance of Anode Materials for High Energy Density Lithium-Ion Batteries through $Sn(SnO_2)$−SiO_2/Graphene-Based Nanocomposites Prepared by a Facile and Low-Cost Approach. *Sustainable Energy Fuels* **2020**, *4*, 4625−4636.
(27) Jarulertwathana, N.; Laokawee, V.; Susingrat, W.; Hwang, S.-J.; Sarakonsri, T. Nano-Structure Tin/Nitrogen-Doped Reduced Graphene Oxide Composites as High Capacity Lithium-Ion Batteries Anodes. *J. Mater. Sci.: Mater. Electron.* **2017**, *28*, 18994−19002.
(28) Yin, H.; Luo, J.; Yang, P.; Yin, P. Aqueous Solution Synthesis of Reduced Graphene Oxide-Germanium Nanoparticles and Their Electrical Property Testing. *Nanoscale Res. Lett.* **2013**, *8*, 1−7.
(29) Harada, Y.; Hoshina, K.; Inagaki, H.; Takami, N. Influence of Synthesis Conditions on Crystal Formation and Electrochemical Properties of TiO_2(B) Particles as Anode Materials for Lithium-Ion Batteries. *Electrochim. Acta* **2013**, *112*, 310−317.
(30) Okumura, T.; Fukutsuka, T.; Yanagihara, A.; Orikasa, Y.; Arai, H.; Ogumi, Z.; Uchimoto, Y. Electronic and Local Structural Changes with Lithium-Ion Insertion in TiO_2-B: X-Ray Absorption Spectroscopy Study. *J. Mater. Chem.* **2011**, *21*, 15369−15377.
(31) Armstrong, A. R.; Arrouvel, C.; Gentili, V.; Parker, S. C.; Islam, M. S.; Bruce, P. G. Lithium Coordination Sites in Li_xTiO_2(B): A Structural and Computational Study. *Chem. Mater.* **2010**, *22*, 6426−6432.
(32) Chimupala, Y.; Drummond-Brydson, R. Hydrothermal Synthesis and Phase Formation Mechanism of TiO_2(B) Nanorods via Alkali Metal Titanate Phase Transformation. *Solid State Phenom.* **2018**, *283*, 23−36.
(33) Sun, S.; Deng, T.; Ding, H.; Chen, Y.; Chen, W. Preparation of Nano-TiO_2-Coated SiO_2 Microsphere Composite Material and Evaluation of Its Self-Cleaning Property. *Nanomaterials* **2017**, *7*, 367.
(34) Zhang, H.; Sun, S.; Ding, H.; Deng, T.; Wang, J. Effect of Calcination Temperature on the Structure and Properties of SiO_2 Microspheres/Nano-TiO_2 Composites. *Mater. Sci. Semicond. Process.* **2020**, *115*, 105099.
(35) Chen, Y.; Ding, H.; Sun, S. Preparation and Characterization of ZnO Nanoparticles Supported on Amorphous SiO_2. *Nanomaterials* **2017**, *7*, 217.
(36) Eddy, D. R.; Ishmah, S. N.; Permana, M. D.; Firdaus, M. L. Synthesis of Titanium Dioxide/Silicon Dioxide from Beach Sand as Photocatalyst for Cr and Pb Remediation. *Catalysts* **2020**, *10*, 1248.
(37) Le Vot, S.; Dambournet, D.; Groult, H.; Ngo, A.-t.; Petit, C.; Rizzi, C.; Salzemann, C.; Sirieix-Plenet, J.; Borkiewicz, O. J.; Raymundo-Piñero, E.; Gaillon, L. Synthesis of Tin Nanocrystals in Room Temperature Ionic Liquids. *Dalton Trans.* **2014**, *43*, 18025−18034.
(38) Lu, M.; Cheng, H.; Yang, Y. A Comparison of Solid Electrolyte Interphase (SEI) on the Artificial Graphite Anode of the Aged and Cycled Commercial Lithium Ion Cells. *Electrochim. Acta* **2008**, *53*, 3539−3546.
(39) Jin, Y.; Li, S.; Kushima, A.; Zheng, X.; Sun, Y.; Xie, J.; Sun, J.; Xue, W.; Zhou, G.; Wu, J.; Shi, F.; Zhang, R.; Zhu, Z.; So, K.; Cui, Y.; Li, J. Self-Healing SEI Enables Full-Cell Cycling of a Silicon-Majority Anode with a Coulombic Efficiency Exceeding 99.9. *Energy Environ. Sci.* **2017**, *10*, 580−592.
(40) Blanco, M. V.; Renman, V.; Vullum-Bruer, F.; Svensson, A. M. Nanostructured Diatom Earth SiO_2 Negative Electrodes with Superior Electrochemical Performance for Lithium Ion Batteries. *RSC Adv.* **2020**, *10*, 33490−33498.
(41) Ding, X.; Liang, D.; Zhao, H. Enhanced Electrochemical Performance Promoted by Tin in Silica Anode Materials for Stable and High-Capacity Lithium-Ion Batteries. *Materials* **2021**, *14*, 1071.
(42) Autthawong, T.; Chimupala, Y.; Haruta, M.; Kurata, H.; Kiyomura, T.; Yu, A.-s.; Chairuangsri, T.; Sarakonsri, T. Ultrafast-Charging and Long Cycle-Life Anode Materials of TiO_2-Bronze/Nitrogen-Doped Graphene Nanocomposites for High-Performance Lithium-Ion Batteries. *RSC Adv.* **2020**, *10*, 43811−43824.
(43) Li, Z.; Zhao, H.; Lv, P.; Zhang, Z.; Zhang, Y.; Du, Z.; Teng, Y.; Zhao, L.; Zhu, Z. Watermelon-Like Structured SiOx−TiO2@C Nanocomposite as a High-Performance Lithium-Ion Battery Anode. *Adv. Funct. Mater.* **2018**, *28*, 1605711.
(44) Han, Y.; Liu, X.; Lu, Z. Systematic Investigation of Prelithiated SiO_2 Particles for High-Performance Anodes in Lithium-Ion Battery. *Appl. Sci.* **2018**, *8*, 1245.
(45) Yan, N.; Wang, F.; Zhong, H.; Li, Y.; Wang, Y.; Hu, L.; Chen, Q. Hollow Porous SiO_2 Nanocubes Towards High-Performance Anodes for Lithium-Ion Batteries. *Sci. Rep.* **2013**, *3*, 1568.
(46) Li, W.; Wang, F.; Ma, M.; Zhou, J.; Liu, Y.; Chen, Y. Preparation of SiO_2 Nanowire Arrays as Anode Material with Enhanced Lithium Storage Performance. *RSC Adv.* **2018**, *8*, 33652−33658.
(47) Ma, X.; Wei, Z.; Han, H.; Wang, X.; Cui, K.; Yang, L. Tunable Construction of Multi-Shell Hollow SiO_2 Microspheres with Hierarchically Porous Structure as High-Performance Anodes for Lithium-Ion Batteries. *Chem. Eng. J.* **2017**, *323*, 252−259.
(48) Kurc, B. $Li_4Ti_5O_{12}$/TiO_2-SiO_2 and Li4Ti5O12/SiO2 Composites as an Anode Material for Li-Ion Batteries. *Ionics* **2018**, *24*, 121−131.
(49) Pineda-Aguilar, N.; Sánchez-Domínguez, M.; Sánchez-Cervantes, E. M.; Garza-Tovar, L. L. Preparation of TiO_2-(B)/SnO_2 Nanostructured Composites and Its Performance as Anodes for Lithium-Ion Batteries. *J. Mater. Res.* **2020**, *35*, 2491−2505.
(50) Zukalová, M.; Kalbáč, M.; Kavan, L.; Exnar, I.; Haeger, A.; Graetzel, M. Electrochemical and Gas-Phase Photocatalytic Performance of Nanostructured TiO2(B) Prepared by Novel Synthetic Route. *Prog. Solid State Chem.* **2005**, *33*, 253−261.
(51) Xin, F.; Whittingham, M. S. Challenges and Development of Tin-Based Anode with High Volumetric Capacity for Li-Ion Batteries. *Electrochem. Energy Rev.* **2020**, *3*, 643−655.
(52) Mou, H.; Xiao, W.; Miao, C.; Li, R.; Yu, L. Tin and Tin Compound Materials as Anodes in Lithium-Ion and Sodium-Ion Batteries: A Review. *Front. Chem.* **2020**, *8*, 141.
(53) Ocon, J. D.; Lee, J. K.; Lee, J. High Energy Density Germanium Anodes for next Generation Lithium Ion Batteries. *Appl. Chem. Eng.* **2014**, *25*, 1−13.
(54) Hu, Z.; Zhang, S.; Zhang, C.; Cui, G. High Performance Germanium-Based Anode Materials. *Coord. Chem. Rev.* **2016**, *326*, 34−85.
(55) Wang, B.; Jin, J.; Hong, X.; Gu, S.; Guo, J.; Wen, Z. Facile Synthesis of the Sandwich-Structured Germanium/Reduced Graphene Oxide Hybrid: An Advanced Anode Material for High-Performance Lithium Ion Batteries. *J. Mater. Chem. A* **2017**, *5*, 13430−13438.
(56) Wang, Y.; Zhang, J. Ultrafine TiO_2(B) Nanowires for Ultrahigh-Rate Lithium-Ion Batteries. *Ionics* **2020**, *26*, 1159−1164.

https://doi.org/10.1021/acsomega.1c05982
ACS Omega 2022, 7, 1357−1367

(57) Armstrong, G.; Armstrong, A. R.; Canales, J.; Bruce, P. G. TiO_2(B) Nanotubes as Negative Electrodes for Rechargeable Lithium Batteries. *Electrochem. Solid-State Lett.* **2006**, *9*, A139.
(58) Kim, N.; Raj, M. R.; Lee, G. Nitrogen-Doped TiO_2(B) Nanobelts Enabling Enhancement of Electronic Conductivity and Efficiency of Lithium-Ion Storage. *Nanotechnology* **2020**, *31*, 415401.
(59) Sinebryukhov, S. L.; Opra, D. P.; Sokolov, A. A.; Podgorbunsky, A. B.; Gnedenkov, S. V. Zirconium-Doped TiO_2(B) Anode for Advanced Li-Ion Batteries. *The 29th International Ocean and Polar Engineering Conference, June 16, 2019*, 2019.
(60) Cui, P.; Xie, B.; Li, X.; Li, M.; Li, Y.; Wang, Y.; Liu, Z.; Liu, X.; Huang, J.; Song, D.; Mbengue, J. M. Anatase/TiO_2-B Hybrid Microspheres Constructed from Ultrathin Nanosheets: Facile Synthesis and Application for Fast Lithium Ion Storage. *CrystEngComm* **2015**, *17*, 7930−7937.
(61) Li, K.; Li, B.; Wu, J.; Kang, F.; Kim, J.-K.; Zhang, T.-Y. Ultrafast-Charging and Long-Life Li-Ion Battery Anodes of TiO_2-B and Anatase Dual-Phase Nanowires. *ACS Appl. Mater. Interfaces* **2017**, *9*, 35917−35926.
(62) Wang, J.-F.; Zhang, J.-J.; He, D.-N. Flower-like TiO_2-B Particles Wrapped by Graphene with Different Contents as an Anode Material for Lithium-Ion Batteries. *Nano-Struct. Nano-Objects* **2018**, *15*, 216−223.
(63) Tang, Y. P.; Wang, S. M.; Ding, J. F.; Hou, G. Y.; Zheng, G. Q. Preparation and Properties of TiO_2(B)/Graphene Nanocomposites as Anode Materials Fo Lithium-Ion Batteries. *Adv. Mater. Res.* **2014**, *875*−*877*, 183−186.
(64) Hou, J.; Wu, R.; Zhao, P.; Chang, A.; Ji, G.; Gao, B.; Zhao, Q. Graphene−TiO_2(B) Nanowires Composite Material: Synthesis, Characterization and Application in Lithium-Ion Batteries. *Mater. Lett.* **2013**, *100*, 173−176.
(65) Yang, Z.; Du, G.; Guo, Z.; Yu, X.; Chen, Z.; Guo, T.; Liu, H. TiO_2(B)@carbon Composite Nanowires as Anode for Lithium Ion Batteries with Enhanced Reversible Capacity and Cyclic Performance. *J. Mater. Chem.* **2011**, *21*, 8591−8596.

https://doi.org/10.1021/acsomega.1c05982
ACS Omega 2022, 7, 1357−1367